



1 Ecosystem Climate Sensitivities Drive the Divergence in
2 Aerosol-Induced Carbon Uptake Across CMIP6 Models

3 Zhaoyang Zhang¹, Meng Fan^{2*}, Minghui Tao³, Yunhui Tan⁴, Quan Wang⁵

4 1. College of Geography and Environmental Sciences, Zhejiang Normal University,
5 Zhejiang Province 321000, China

6 2. Aerospace Information Research Institute, Chinese Academy of Sciences, Beijing
7 100101, China

8 3. School of Geography and Information Engineering, China University of
9 Geosciences, Wuhan 430074, China

10 4. School of Computer Science, China University of Geosciences, Wuhan 430078,
11 China

12 5. Faculty of Agriculture, Shizuoka University, Shizuoka 4228529, Japan

13 *Corresponding author: Meng Fan (fanmeng@aircas.ac.cn)

14

15

16



17 **Abstract**

18 Anthropogenic aerosols significantly affect the terrestrial carbon cycle. Many
19 models have been developed to simulate the effects of aerosols on regional ecosystem
20 productivity. However, the differences among models in simulating the impacts of
21 aerosols on gross primary production (GPP) remain unclear. To investigate the response
22 of GPP to aerosol loadings among different models, we analyzed historical and hist-
23 piAer simulations from five Earth System Models (ESMs) in Coupled Model
24 Intercomparison Project Phase 6 (CMIP6). The results showed that all models captured
25 the decrease in GPP (mean: $-0.059 \text{ gC m}^{-2}\text{d}^{-1}$) and the magnitudes of aerosol-induced
26 GPP changes varied greatly (-0.019 to $-0.077 \text{ gC m}^{-2}\text{d}^{-1}$). To analyze the roles of aerosol
27 representations and model sensitivities to climatic factors across ESMs, we developed
28 a biophysical attribution framework. Our results showed that inter-model discrepancies
29 in simulating the effects of aerosols on GPP were primarily driven by the differences in
30 ecosystem climate sensitivities across ESMs, especially the response of photosynthesis
31 to radiation and temperature. These findings are very important for fully understanding
32 the impacts of human activities on the terrestrial ecosystem carbon cycle.

33 **Keywords:** gross primary production (GPP); aerosols; earth system models (ESMs);
34 CMIP6

35

36



37 **1. Introduction**

38 Terrestrial gross primary production (GPP) is the largest carbon flux in global
39 carbon cycle (Anav et al., 2015; Lai et al., 2024). Understanding the response of GPP
40 to various environmental factors is critical for accurately simulating the photosynthesis
41 of terrestrial ecosystem (Piao et al., 2008; Huang et al., 2019). Atmospheric aerosol
42 loadings have significantly increased after the Industrial Revolution due to the
43 increased combustion of fossil fuels (Liu et al., 2022). The increased aerosol loadings
44 significantly affect the amount of solar radiation reaching the Earth's surface (Tan et al.,
45 2023), cloud properties (Manshausen et al., 2022), and regional climate (Najafi et al.,
46 2015; Leung and Van Den Heever, 2023). Aerosols also play an important role in the
47 photosynthesis of terrestrial ecosystems by altering the vegetation growing
48 environment, such as radiation and temperature (Zhang et al., 2023b; Zhang et al.,
49 2019).

50 Atmospheric aerosols can affect GPP through four pathways. First, increasing
51 aerosols can reduce the incoming radiation by absorbing and scattering the sunlight
52 (Wu et al., 2025). Second, aerosol loadings also increase the fraction of diffuse radiation
53 (DF) reaching the Earth's surface. The increased DF can enhance the canopy light-use
54 efficiency (LUE) (Gu et al., 2003; Gu et al., 2002). Third, aerosols can also influence
55 the total radiation and DF reaching the surface by affecting the cloud properties (Khatri
56 et al., 2021). Furthermore, aerosols also influence the terrestrial ecosystem
57 photosynthesis through altering the air temperature and precipitation (Wang et al., 2018;
58 Zhang et al., 2021a). To quantify the effect of aerosols on GPP, ground-based
59 measurements and model simulations have been widely used.

60 Ground-based measurements provided some insights into the effect of aerosols on
61 GPP at site scale. These studies showed that the increased aerosol loadings enhanced
62 the canopy LUE by reducing the light saturation in the upper layers and enhancing
63 photosynthesis in the lower canopy layers (Gu et al., 2002; Gu et al., 2003). Niyogi et
64 al. (2004) showed that the effect of diffuse radiation induced by clouds and aerosols on
65 canopy LUE varied with the vegetation types due to the canopy structure. Ground-based



66 measurements also showed that the enhanced photosynthetic rates of sunlit and shaded
67 leaves under high aerosol loadings conditions were driven by different environmental
68 factors. The enhanced photosynthesis for sunlit and shaded leaves are induced by lower
69 vapor pressure deficit (VPD) and higher diffuse radiation, respectively (Wang et al.,
70 2018).

71 To investigate the changes of regional GPP induced by aerosols, model simulations
72 were conducted. For example, Mercado et al. (2009) and Rap et al. (2018) showed that
73 anthropogenic aerosols enhanced land carbon uptake due to the diffuse fertilization
74 effects (DFE). Yue and Unger (2017) showed that the aerosol-induced change in net
75 primary productivity (NPP) over China was from -3% to 6% depending on the local
76 aerosol optical depth (AOD). However, these studies did not account for indirect
77 aerosol radiative effects and aerosol climatic effects. To comprehensively understand
78 the impact of aerosols, many other modelling studies were conducted. For example,
79 Zhang et al. (2021a) reported that aerosols enhanced vegetation carbon dioxide sink
80 since 1850 due to the DFE and cooling effects induced by aerosols. Zhang et al. (2023a)
81 found that aerosols caused 0.43% reduction in net biome production from 1980 to 2014
82 using the Community Earth System Model (CESM, version 2.1.3) and the dominant
83 variable is the changes of temperature. Zhou et al. (2024) simulated the impact of the
84 Clean Air Action plan on ecosystem carbon assimilation and found that aerosol
85 reductions led to NPP increase of $20.1 \pm 10.9 \text{ TgCyr}^{-1}$ and the aerosol climatic effects on
86 NPP are twice that of the aerosol radiative effects. These studies indicated that there
87 were still large uncertainties in simulating the effects of aerosols on GPP (Liu et al.,
88 2021; Zhang et al., 2021b).

89 The uncertainties of aerosol-induced GPP changes could be induced by aerosol
90 direct and indirect effects and model sensitivities to climatic factors (defined as the
91 ecosystem climate sensitivity). Bellouin et al. (2020) reported that there were large
92 uncertainties in simulating aerosol radiative forcing. Additionally, many studies
93 demonstrated that the parameterization of vegetation photosynthesis within Earth
94 System Models (ESMs) also have large uncertainties (Hu et al., 2022; Gier et al., 2024).



95 Liu et al. (2021) showed that current LUE models have large bias in estimating the DFE.
96 However, it remains unclear whether the impact of aerosols on GPP simulated by
97 different ESMs is consistent and the dominant factors driving divergence among
98 different ESMs remain unclear. In this study, we used simulations with and without
99 anthropogenic aerosol emissions from the Coupled Model Intercomparison Project
100 Phase 6 (CMIP6). Our objectives of this study were: (1) to quantify the consistency
101 among CMIP6 models in estimating the impacts of aerosols on terrestrial GPP; (2) to
102 explore the contributor for inter-model differences. This multi-model assessment will
103 enhance our understanding of the interactions between anthropogenic aerosols, climate,
104 and terrestrial ecosystems.

105 **2. Data and method**

106 **2.1 CMIP6 simulations**

107 To investigate the effect of anthropogenic aerosols on terrestrial GPP, we used the
108 paired simulations from the Aerosol and Chemistry Model Intercomparison Project
109 (AerChemMIP), a CMIP6-endorsed activity (Collins et al., 2017). We selected five
110 Earth System Models (ESMs), including BCC-ESM1, IPSL-CM6A-LR, NorESM2-
111 LM, MPI-ESM-1-2-HAM, and UKESM1-0-LL. These models have a diverse range of
112 land surface components. Four of five models considered the differential effects of
113 direct and diffuse radiation on canopy photosynthesis (Table 1). For each model, we
114 compared the historical experiment against the hist-piAer experiment from 1850 to
115 2014. The historical experiment is driven by all time-evolving natural and
116 anthropogenic forcings, while the hist-piAer experiment is run in parallel with the
117 historical experiment but fixes the anthropogenic aerosol emissions at pre-industrial
118 levels. This experimental design can be used to calculate the variations of GPP induced
119 by aerosols.

120 The monthly GPP, surface downwelling shortwave radiation (rsds), near-surface
121 air temperature (tas), top-of-atmosphere incident shortwave radiation (rsdt),
122 precipitation (pr), total cloud cover percentage (clt), aerosol optical depth at 550nm
123 (od550aer) from historical and hist-piAer experiments were used in this study. The



124 model simulations can be downloaded from Earth System Grid Federation (ESGF).
125 Only NorESM2-LM and UKESM1-0-LL historical experiments provide diffuse
126 radiation datasets. To illustrate the impact of DF on vegetation photosynthesis, we
127 calculated the clearness index (CI, $rsds/rsdt$). Previous study demonstrated that CI was
128 strongly correlated with DF (Zhang et al., 2023c). We also show the scatter plots of DF
129 against CI from these two models (Fig. S1). The results also indicate that there is a very
130 high correlation between these two variables ($R^2=0.727$). All data were regridded to a
131 resolution of $1.25^\circ \times 2.5^\circ$ (latitude by longitude). The impact of aerosols on GPP was
132 isolated by comparing historical and hist-piAer scenarios (historical-hist-piAer).
133 Table 1. CMIP6 Earth system models (ESMs) used in this study. For each model, the land component
134 model and whether the model accounts for the diffuse fertilization effect (DFE) on canopy photosynthesis
135 or not are listed.

Model	Land component	DFE	References
IPSL-CM6A-LR	ORCHIDEE v2.0	NO	(Boucher et al., 2020)
MPI-ESM-1-2-HAM	JSBACH 3.20	YES	(Reick et al., 2021; Mauritsen et al., 2019)
NorESM2-LM	CLM	YES	(Lawrence et al., 2011; Lawrence et al., 2019)
BCC-ESM1	BCC_AVIM2	YES	(Li et al., 2019; Wu et al., 2020)
UKESM1-0-LL	JULES-ES-1.0	YES	(Sellar et al., 2019; Clark et al., 2011)

136 2.2 Observational data for model validation

137 In this study, monthly eddy covariance flux measurements from FLUXNET were
138 used to assess the performance of GPP from CMIP6 ESMs. FLUXNET is a global
139 network of eddy covariance towers, which can provide measured data on energy, water,



140 and carbon dioxide exchanges between the biosphere and atmosphere (Pastorello et al.,
141 2020). In this study, we used datasets from FLUXNET2015, which has over 1,500 site-
142 years of measurements from 212 locations (Lasslop et al., 2010). We utilized data
143 records containing more than 80% of measured values and good quality gap-filled data
144 ($NEE_VUT_REF_QC \geq 0.8$) to ensure the quality of GPP. Fig. S2 shows monthly GPP
145 from five CMIP6 models (a-e) against FLUXNET site observations. The results reveal
146 a systematic underestimation of high GPP (slopes 0.406–0.632) and low coefficient of
147 determination ($R^2=0.305-0.438$) at the site scale. Additionally, we also used the
148 FLUXCOM-X products to evaluate the simulated GPP from CMIP6 ESMs.
149 FLUXCOM-X is the global terrestrial GPP and evapotranspiration (ET) products
150 derived from a newly data-driven scaling framework (X-BASE) (Nelson et al., 2024).
151 Nelson et al. (2024) demonstrated that the X-BASE dataset was significantly improved
152 compared to previous versions of FLUXCOM. The FLUXCOM-X products were also
153 regridded into 1.25° in latitude and 2.5° in longitude. Fig. S3 shows the performance of
154 monthly GPP from five CMIP6 ESMs (a-e) against the FLUXCOM-X GPP. The
155 coefficients of determination (R^2) for these models range from 0.517 to 0.678, with root
156 mean square errors (RMSEs) between 1.642 and 2.563 $gC\ m^{-2}\ d^{-1}$. The spatial
157 distribution of observed and simulated GPP from 2001 to 2014 were also shown in Fig.
158 S4.

159 **2.3 Attribution Framework of Inter-Model Spread**

160 The inter-model spread is attributed to discrepancies in simulated aerosol radiative
161 and climatic effects and the sensitivities of model to climatic factors. To quantify the
162 sources of uncertainty in aerosol-induced GPP changes (ΔGPP), we developed an
163 attribution framework based on the method of Yu and Huang (2023). The framework is
164 based on the biophysical principle that GPP is the product of photosynthetically active
165 radiation (PAR), fraction of absorbed PAR (fPAR) and LUE. GPP can be calculated as
166 follows:

$$167 \quad GPP = PAR * fPAR * LUE(tas, pr, CI) \quad (1)$$

168 where LUE is dependent on environmental conditions including *tas*, *pr*, and *CI*.



169 To mathematically represent the aerosol-induced anomaly, a first-order Taylor
 170 expansion is applied to Equation (1):

$$171 \quad \delta GPP \approx fPAR * LUE * \delta PAR + PAR * \delta(fPAR * LUE) \quad (2)$$

172 Zhang et al. (2024) and Shao et al. (2020) reported that DFE was primarily driven by
 173 improved LUE rather than by light absorption. Therefore, Equation 2 can be rewritten
 174 as:

$$175 \quad \delta GPP \approx fPAR * LUE * \delta PAR + PAR * fPAR * \delta LUE \quad (3)$$

176 Bloomfield et al. (2022) showed that a generalized linear mixed-effects model could
 177 well represent the response of LUE to environmental factors. In addition, aerosol-
 178 induced changes in climatic variables are small. Therefore, the change in LUE (δLUE)
 179 can be approximated linearly:

$$180 \quad \delta LUE \approx \frac{\partial LUE}{\partial tas} \delta tas + \frac{\partial LUE}{\partial pr} \delta pr + \frac{\partial LUE}{\partial CI} \delta CI \quad (4)$$

181 Substituting Equation (4) into Equation (3) can get the full decomposition:

$$182 \quad \delta GPP \approx fPAR * LUE * \delta PAR + \frac{\partial LUE}{\partial tas} * fPAR * PAR * \delta tas + \frac{\partial LUE}{\partial pr} * fPAR *
 183 \quad \quad \quad PAR * \delta pr + \frac{\partial LUE}{\partial CI} * fPAR * PAR * \delta CI \quad (5)$$

184 A multivariate regression model was constructed for specific plant functional type
 185 (PFT) and ESM to capture the impacts of climatic drivers and systematic model biases.
 186 The regression equation for a specific model (m) is defined as:

$$187 \quad \delta GPP_m \approx \beta_{0,m} + \beta_{1,m} \delta PAR_m + \beta_{2,m} PAR_{clim} * \delta tas_m + \beta_{3,m} PAR_{clim} * \delta pr_m + \beta_{4,m} PAR_{clim} * \delta CI_m \quad (6)$$

188 Here, δGPP_m represents the aerosol-induced anomaly of GPP (Historical-Hist-piAer)
 189 from model m . PAR_{clim} is the climatological baseline PAR (0.45*rads). β_1 is the
 190 product of fPAR and LUE. β_{2-4} represents the product of fPAR and the partial
 191 derivatives of LUE to climatic factors, while the intercept β_0 represents the systematic
 192 bias of the model. To address multicollinearity, standardized ridge regression was used
 193 for the specific PFT.

194 To quantify the inter-model divergence, we calculated the deviation of model m
 195 from the multi-model ensemble mean (mmm) by using the Equation 6.

$$196 \quad \Delta(\delta GPP) = \delta GPP_m - \delta GPP_{mmm} \quad (7)$$



197 By substituting the regression equations into Equation 7 and rearranging terms, we
198 derived the final equation:

$$199 \quad \Delta(\delta GPP) = \underbrace{\sum_i \beta_{i,mmm}(X_{i,m} - X_{i,mmm})}_{\text{State contribution}} + \underbrace{\sum_i X_{i,m}(\beta_{i,m} - \beta_{i,mmm}) + (\beta_{0,m} - \beta_{0,mmm})}_{\text{Sensitivity contribution}} \quad (8)$$

200 where X_i represents the independent variables (including interaction terms). This
201 equation decomposes the model spread into two components:

202 (1) State contribution: The divergence arising from differences in the simulated aerosol
203 radiative and climatic effects (e.g., differences in simulated pr: $X_{i,m} - X_{i,mmm}$),
204 weighted by the mean pr sensitivity ($\beta_{i,mmm}$).

205 (2) Sensitivity contribution: The divergence arising from ecosystem climate
206 sensitivities across ESMs. This term represents the contributions from dynamic
207 photosynthesis sensitivity differences ($\beta_{i,m} - \beta_{i,mmm}$) and the systematic bias
208 differences ($\beta_{0,m} - \beta_{0,mmm}$).

209 **3. Results**

210 **3.1 The changes of global GPP induced by aerosols**

211 Fig. 1 shows the spatial patterns of aerosol-induced changes in GPP from five
212 CMIP6 ESMs and their multi-model mean. In the multi-model ensemble mean (Fig.
213 1a), aerosol loadings lead to a reduction in GPP ($0.0586 \text{ gC m}^{-2}\text{d}^{-1}$), with 70.31% of
214 global land areas experiencing decreased GPP. Notably, the Northern and Southern
215 Hemispheres exhibit contrasting responses: most areas in the Northern Hemisphere
216 show decreased GPP, whereas some regions in the Southern Hemisphere show modest
217 increases. The results suggest that the changes of GPP induced by aerosols in Northern
218 and Southern Hemispheres are asymmetric. Large positive GPP anomalies can be
219 observed around 30°S , while a pronounced decline in GPP is shown around 70°N .

220 Among the individual models, BCC-ESM1 shows the general spatial pattern of the
221 multi-model ensemble mean but exhibits stronger regional variability. More areas show
222 positive GPP anomalies in BCC-ESM1 than in the multi-model ensemble mean over
223 the Northern Hemisphere. Weak aerosol effects are simulated by IPSL-CM6A-LR with
224 small changes in GPP. In contrast, MPI-ESM1-2-HAM model reveals large GPP
225 reductions across central and southern China, western Europe, and the eastern United



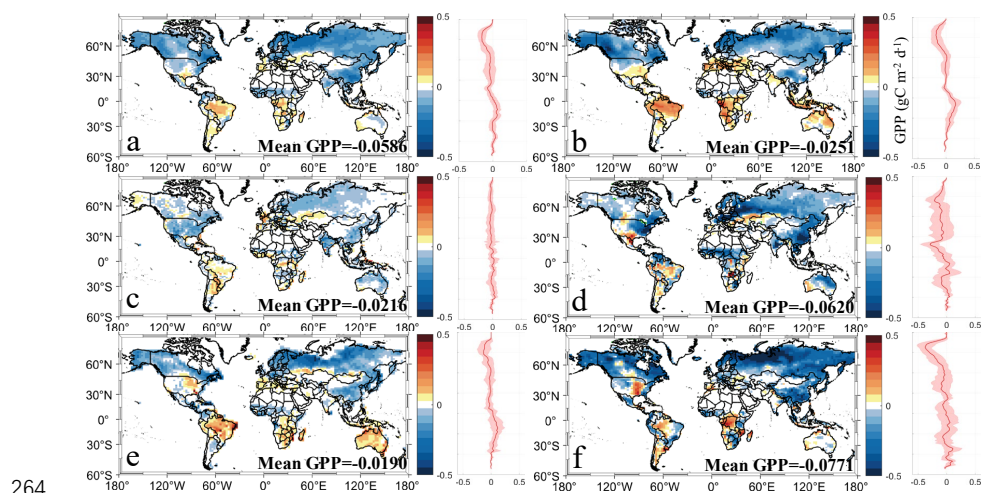
226 States. All these regions have relatively high aerosol emissions. NorESM2-LM shows
227 increased GPP in some areas of South America and decreased GPP over Europe.
228 UKESM1-0-LL shows increased GPP in the eastern United States, central Africa, and
229 parts of South America and decreased GPP across northern Europe and Asia.

230 In these models, decreased GPP can be found in northern mid-to-high latitudes and
231 eastern China. The result shows a robust signal of aerosol-induced suppression of
232 photosynthesis in these regions. There are 58.18%, 68.64%, 77.91%, 53.86%, and 72.94%
233 of the global regions showing reduced GPP for BCC-ESM1, IPSL-CM6A-LR, MPI-
234 ESM-1-2-HAM, NorESM2-LM, and UKESM1-0-LL, respectively. The mean aerosol-
235 induced GPP changes is -0.0251, 0.1924, -0.0216, -0.0620, -0.0190, and -0.0771 gC m⁻²
236 d⁻¹ from BCC-ESM1, IPSL-CM6A-LR, MPI-ESM-1-2-HAM, NorESM2-LM, and
237 UKESM1-0-LL, respectively. Although all models show the reduction in GPP, the
238 magnitude and spatial distribution of GPP changes vary greatly among models. These
239 discrepancies suggest the uncertainty in quantifying aerosol impacts on the terrestrial
240 carbon cycle in current ESMs.

241 In all four seasons, the CMIP6 models consistently show negative GPP anomalies
242 induced by aerosols. However, there are large differences in the magnitude and spatial
243 distribution (Fig. S5-8). In March–May, the multi-model ensemble mean reveals
244 widespread GPP reductions over the mid- and high-latitudes of the Northern
245 Hemisphere, particularly across East Asia and Europe. The differences among the
246 models are significant, with BCC-ESM1, MPI-ESM-1-2-HAM, and UKESM1-0-LL
247 simulating stronger reductions, while IPSL-CM6A-LR and NorESM2-LM show
248 weaker responses of GPP to aerosols. During the period of June–August, the variations
249 of GPP are greater and there are more regions showing positive anomalies. The
250 differences among models become more pronounced, especially in the low- and mid-
251 latitudes. For example, simulations from BCC-ESM1 and UKESM1-0-LL show that
252 the impacts of aerosols on GPP are positive in most regions of the United States and
253 Europe, whereas MPI-ESM-1-2-HAM reveals that the GPP anomalies are negative in
254 half of these regions. Meanwhile, the IPSL-CM6A-LR model simulation indicates that



255 the changes of GPP are negative over the United States. In September–November, the
256 negative anomalies are also shown but weaker than that during the period of June–
257 August. Over Australia, the aerosol effects on GPP are positive from BCC-ESM1 and
258 NorESM2-LM, but negative from IPSL-CM6A-LR and MPI-ESM-1-2-HAM. In
259 December–February, aerosols consistently exhibit a small negative effect on GPP in the
260 Northern Hemisphere, whereas model simulations show large discrepancies in the
261 Southern Hemisphere. In all, these results demonstrate that aerosols generally suppress
262 global GPP, but with significant differences in the amplitude and spatial distribution
263 among models.

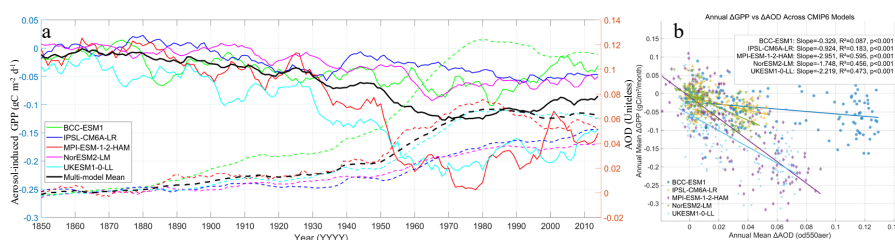


264
265 Figure 1. The spatial pattern of changes in ecosystem GPP ($\text{gC}/(\text{m}^2\text{d})$) induced by aerosols from CMIP6
266 models (a. multi-model mean, b. BCC-ESM1, c. IPSL-CM6A-LR, d. MPI-ESM-1-2-HAM, e.
267 NorESM2-LM, f. UKESM1-0-LL).

268 Fig. 2a shows the time series of the ten-year average changes of GPP induced by
269 aerosols and AOD variations from 1850 to 2014. The results show that global GPP and
270 AOD have experienced large variations. The aerosol-induced GPP changes show a
271 decreasing trend from 1850 to the mid-20th century, with a marked shift around the
272 1950s. This reduction was induced by the increasing aerosol emissions. From 1850 to
273 1890, some models show a positive impact of aerosols on GPP due to the very low
274 AOD. After 1980, an increase in GPP can be observed. This aligns with the decreasing



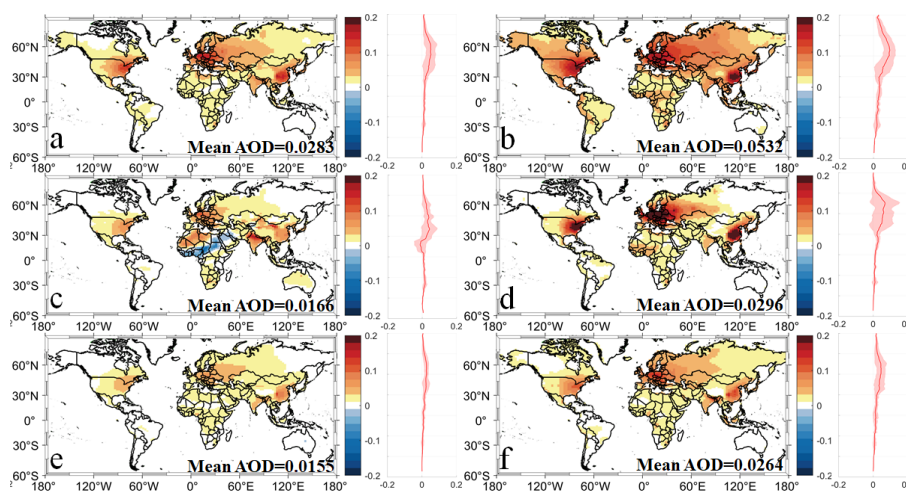
275 aerosol loadings. There are notable differences between the models in the magnitude
276 and timing of GPP and AOD changes. MPI-ESM-1-2-HAM and UKESM1-0-LL
277 exhibit a larger variation of GPP compared to the other models. Fig. 2b shows that the
278 scatter plots of annual mean of GPP changes induced by aerosols against the AOD
279 variations. Aerosol-induced changes in GPP are significantly related to the AOD
280 ($p < 0.001$). However, the sensitivities of GPP to aerosol loadings are different among
281 models. These discrepancies highlight the uncertainty in simulating atmospheric
282 aerosol loadings and the impact of aerosols on global productivity.



283 Figure 2. (a) Time series of aerosol-induced GPP changes (solid lines) and AOD variations (dashed
284 lines) from 1850 to 2014 with a ten-years moving window; (b) The scatter plots of annual mean of
285 GPP changes induced by aerosols against the AOD variations.

287 3.2 Changes of aerosols and meteorological factors

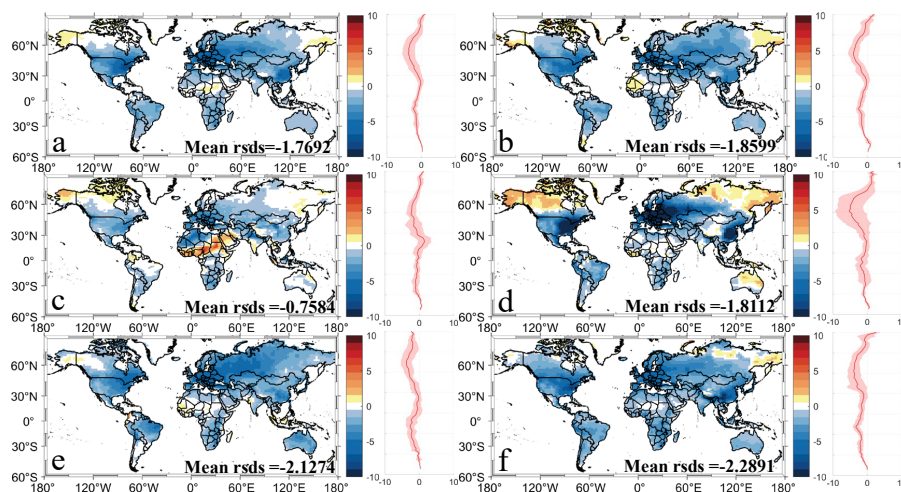
288 Analysis of AOD differences at 550 nm (od550aer) between historical and hist-
289 piAer experiments reveals significant discrepancies among CMIP6 ESMs (Fig. 3). The
290 multi-model ensemble mean differences in AOD (Fig. 3a) show significant increase in
291 AOD across northern mid-latitudes, especially in major industrial regions including
292 North America, Europe, and East Asia. In contrast, IPSL-CM6A-LR (Fig. 3c) shows
293 decreased AOD in some regions. MPI-ESM-1-2-HAM (Fig. 3d) and UKESM1-0-LL
294 (Fig. 3f) show high aerosol loadings in industrialized regions of North America and
295 Eurasia. NorESM2-LM (Fig. 3e) shows a relatively modest aerosol increase. The
296 spatial distribution of AOD reveals substantial inter-model discrepancies in simulating
297 the global aerosol loadings.



298

299 Figure 3. The spatial pattern of mean differences of aerosol optical depth (AOD) at 550nm (od550aer)
300 between historical and hist-piAer experiments over the period 1850–2014 (a. multi-model mean, b. BCC-
301 ESM1, c. IPSL-CM6A-LR, d. MPI-ESM-1-2-HAM, e. NorESM2-LM, f. UKESM1-0-LL).

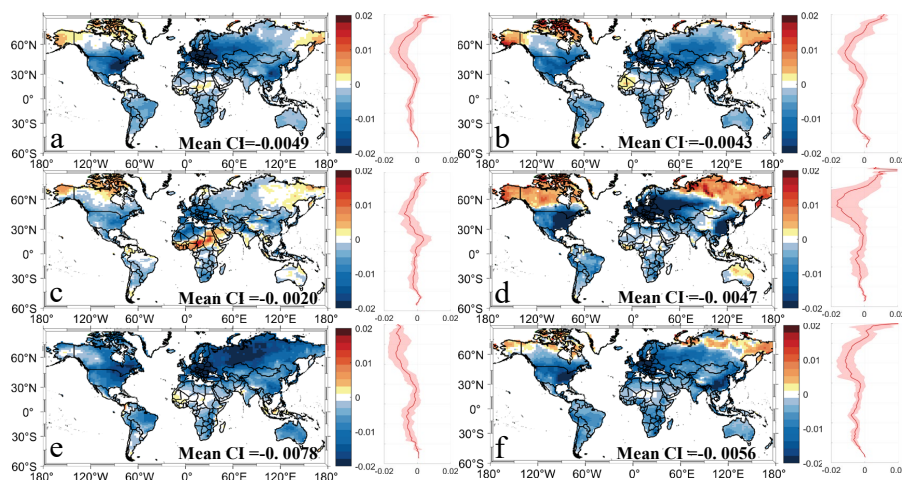
302 Analysis of mean differences in rsds between historical and hist-piAer scenarios
303 further demonstrates pronounced inter-model variability (Fig. 4). The multi-model
304 ensemble mean differences in rsds (Fig. 4a) show reduction in most of the regions,
305 especially in northern mid-latitudes. Models such as BCC-ESM1 (Fig. 4b) and
306 UKESM1-0-LL (Fig. 4f) show similar spatial distribution of variations in rsds. Among
307 all models, MPI-ESM-1-2-HAM (Fig. 4d) has the largest area where rsds increases.
308 NorESM2-LM (Fig. 4e) show widespread decreases. IPSL-CM6A-LR (Fig. 4c)
309 presents a more complex spatial distribution, highlighting reductions in shortwave
310 radiation over parts of Eurasia and Africa but also notable regional increases. This is
311 consistent with the spatial distribution of AOD. The result shows that there are large
312 differences among ESMs in simulating radiation.



313

314 Figure 4. The spatial distribution of mean differences of shortwave radiation (rsds, W/m^2) between
315 historical and hist-piAer experiments from 1850 to 2014 (a. multi-model mean, b. BCC-ESM1, c. IPSL-
316 CM6A-LR, d. MPI-ESM1-2-HAM, e. NorESM2-LM, f. UKESM1-0-LL).

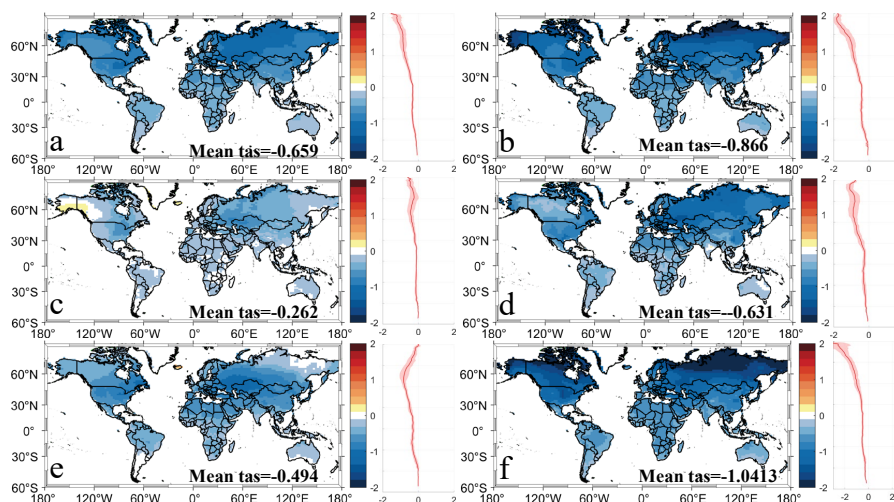
317 The spatial distribution of mean differences in the CI between historical and hist-
318 piAer scenarios is consistent with that of rsds. BCC-ESM1 (Fig. 5b) and UKESM1-0-
319 LL (Fig. 5f) show the decreases in CI in most regions. The CI decreases significantly
320 in northern mid-latitude regions with the high aerosol loadings. In the NorESM2-LM
321 (Fig. 5e), CI shows a decreasing trend in almost all regions. IPSL-CM6A-LR (Fig. 5c)
322 reveals heterogeneous changes, with localized areas showing increased CI amidst
323 predominant decreases. The result also shows large discrepancies in simulating the
324 variations of CI induced by the aerosols.



325

326 Figure 5. The spatial pattern of mean differences of clearness index (CI) between historical and hist-
327 piAer experiments from 1850 to 2014 (a. multi-model mean, b. BCC-ESM1, c. IPSL-CM6A-LR, d. MPI-
328 ESM-1-2-HAM, e. NorESM2-LM, f. UKESM1-0-LL).

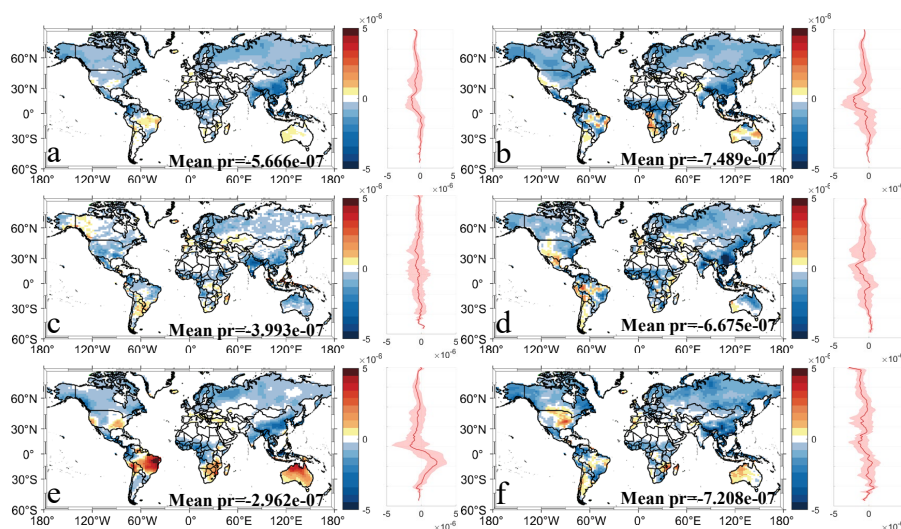
329 The spatial distribution of mean differences in tas between historical and hist-piAer
330 scenarios reveals consistent cooling trends in response to increased aerosol loadings
331 across these models in CMIP6 (Fig. 6). The multi-model ensemble mean differences of
332 tas (Fig. 6a) shows that aerosols can induce the decrease in tas. BCC-ESM1 (Fig. 6b),
333 MPI-ESM-1-2-HAM (Fig. 6d), and UKESM1-0-LL (Fig. 6f) prominently show
334 widespread cooling in the Northern Hemisphere. The tas in high-latitude areas of the
335 Northern Hemisphere decreases more than that in mid- and low-latitude regions. The
336 temperature in the Southern Hemisphere is less affected than that in the Northern
337 Hemisphere. NorESM2-LM (Fig. 6e) and IPSL-CM6A-LR (Fig. 6c) also exhibit
338 decreased tas, but with weaker magnitude.



339

340 Figure 6. The spatial pattern of mean differences of near-surface air temperature (tas, °C) between
341 historical and hist-piAer experiments from 1850 to 2014 (a. multi-model mean, b. BCC-ESM1, c. IPSL-
342 CM6A-LR, d. MPI-ESM1-2-HAM, e. NorESM2-LM, f. UKESM1-0-LL).

343 Analysis of mean differences in pr between historical and hist-piAer scenarios
344 reveals that there are also large differences in simulating the impact of aerosols on pr
345 across CMIP6 models (Fig. 7). The multi-model ensemble mean differences of pr show
346 that aerosols induce a reduction in pr in most regions (Fig. 7a). BCC-ESM1 (Fig. 7b)
347 shows modest decrease in pr across mid-latitudes and tropical regions. In contrast,
348 IPSL-CM6A-LR (Fig. 7c), MPI-ESM1-2-HAM (Fig. 7d), NorESM2-LM (Fig. 7e),
349 and UKESM1-0-LL (Fig. 7f) show complex spatial distribution of pr changes, with
350 both pronounced regional increases and decreases. The response of pr to aerosols
351 suggests that there are some uncertainties in aerosol-cloud interactions. This may also
352 induce the uncertainties in simulating regional hydrological cycles.



353

354 Figure 7. The spatial pattern of mean differences of precipitation (pr, kg/(m²s)) between historical and
355 hist-piAer experiments from 1850 to 2014 (a. multi-model mean, b. BCC-ESM1, c. IPSL-CM6A-LR, d.
356 MPI-ESM1-2-HAM, e. NorESM2-LM, f. UKESM1-0-LL).

357 3.3 Attribution of Inter-Model Spread in aerosol-induced GPP changes

358 We applied the attribution framework to quantify the drivers of inter-model spread
359 in aerosol-induced GPP anomalies. The framework decomposes the total spread into
360 contributions from aerosol radiative and climatic effects (“state”) and ecosystem
361 climate sensitivities (“sensitivity”). The framework captures the variability of aerosol-
362 induced GPP changes for most ESMs, with the R² ranging from 0.243 to 0.699 (Fig. 8c,
363 red line). The framework can explain more than 40% of GPP changes, except for
364 NorESM2-LM. The result suggests that the framework can be used for analyzing the
365 contribution of “state” and “sensitivity”.

366 The decomposition of total spread reveals the dominant driver (Fig. 8c, bars). The
367 GPP anomalies in NorESM2-LM are dominated by state contributions (189.3%). This
368 indicates that the aerosol radiative and climatic effects simulated by this model have a
369 large difference with the ensemble mean. In contrast, the main driver of BCC-ESM1
370 is the sensitivity contributions (225.2%). This implies a divergence in model ecological
371 parameterization. Four of five models show that the sensitivity contribution is higher
372 than the state contribution in the inter-model spread. The inter-model discrepancies in



373 aerosol-induced GPP changes are driven by the parameterization of canopy
374 photosynthesis in the ESMs.

375 Fig. 8a shows the contribution of discrepancies in simulated aerosol radiative and
376 climatic effects across models. IPSL-CM6A-LR shows that radiation anomalies have a
377 large positive contribution ($0.043 \text{ gC m}^{-2}\text{d}^{-1}$). This indicates that this model simulates a
378 weaker aerosol dimming effect than other models (Fig. 4c). This is the primary driver
379 for positive GPP anomalies of IPSL-CM6A-LR. For UKESM1-0-LL, radiation shows
380 a strong negative contribution ($-0.026 \text{ gC m}^{-2}\text{d}^{-1}$). This means that the aerosol-induced
381 dimming effect simulated by UKESM1-0-LL is stronger than those of other models
382 (Fig. 4f). For NorESM2-LM, the interaction between PAR and CI plays a prominent
383 role ($0.033 \text{ gC m}^{-2}\text{d}^{-1}$). The interaction between PAR and CI also plays an important
384 role in IPSL-CM6A-LR, but with a negative effect ($-0.044 \text{ gC m}^{-2}\text{d}^{-1}$).

385 Fig. 8b shows the contribution of ecosystem climate sensitivities to the inter-model
386 spread in GPP anomalies. The parameterization of model canopy photosynthesis will
387 induce the divergence in ecosystem climate sensitivities to temperature, precipitation,
388 and radiation. Large difference in the response of photosynthesis to radiation can be
389 observed. This indicates that the assumption of canopy radiative transfer in the ESMs
390 introduces some differences in the response of photosynthesis to radiation. β_{PAR} and
391 β_{CI} represent the sensitivity of vegetation photosynthesis to light quantity and light
392 quality, respectively. The sensitivities of photosynthesis to CI (β_{CI}) from BCC-ESM1
393 ($0.044 \text{ gC m}^{-2}\text{d}^{-1}$) and UKESM1-0-LL ($0.038 \text{ gC m}^{-2}\text{d}^{-1}$) show positive contributions to
394 GPP anomalies. This suggests that these models simulate a stronger diffuse fertilization
395 effect than the multi-model ensemble mean. For UKESM1-0-LL, the diffuse
396 fertilization effect partially reduces by the covaried decreased PAR (β_{PAR} : -0.043 gC
397 $\text{m}^{-2}\text{d}^{-1}$). IPSL-CM6A-LR shows the opposite pattern with a positive contribution from
398 PAR sensitivity ($0.020 \text{ gC m}^{-2}\text{d}^{-1}$) and a negative contribution from CI sensitivity ($-$
399 $0.024 \text{ gC m}^{-2}\text{d}^{-1}$). This indicates that the assumption of canopy radiative transfer in this
400 model is insensitive to the variations of light quality. The sensitivity of photosynthesis
401 to temperature reveals the different thermal adaptation strategies used in the ESMs.



402 MPI-ESM-1-2-HAM shows the highest positive contribution of temperature (β_{tas} :
 403 $0.064 \text{ gC m}^{-2} \text{ d}^{-1}$). This suggests that this model has a larger GPP gain under aerosol-
 404 induced cooling compared to the multi-model ensemble mean. Conversely, BCC-ESM1
 405 shows a negative contribution of temperature sensitivity ($-0.032 \text{ gC m}^{-2} \text{ d}^{-1}$). This
 406 indicates that the photosynthesis in the model gains less than other ESMs. The
 407 contribution of precipitation sensitivity to GPP anomalies is generally smaller than
 408 other environmental factors across most models. This suggests that the response of
 409 ESMs to precipitation is relatively consistent. BCC-ESM1 and IPSL-CM6A-LR show
 410 a moderate positive contribution of precipitation sensitivity (0.016 and $0.011 \text{ gC m}^{-2} \text{ d}^{-1}$),
 411 while other three models show a small negative contribution. We also calculate the
 412 intercept (residual) term, which can represent the systematic deviation in baseline
 413 productivity from the ensemble mean. For MPI-ESM-1-2-HAM and NorESM2-LM,
 414 the baseline bias shows large negative contributions (-0.056 and $-0.050 \text{ gC m}^{-2} \text{ d}^{-1}$,
 415 respectively). This demonstrates that the offsets in base-state parameterizations (e.g.,
 416 lower V_{cmax} compared to the MMM) is also a major source of uncertainty in
 417 simulating the effect of aerosols on plant productivity.



418

419 Figure 8. Decomposition of drivers governing the inter-model spread in aerosol-induced GPP anomalies.



420 Contributions ($\text{gC m}^{-2}\text{d}^{-1}$) arising from differences in (a) aerosol radiative and climatic effects (State;
421 including ΔPAR and interaction terms) and (b) ecosystem climate sensitivities (Sensitivity; including
422 dynamic $\Delta\beta$ and residual). (c) Aggregated relative contributions (bars) and coefficient of determination
423 (R^2 , line). Components: State (blue), Sensitivity (orange), Residual (green).

424 **4. Discussion**

425 **4.1 Divergent aerosol impacts on terrestrial GPP in CMIP6 models**

426 This study revealed significant inter-model divergence among CMIP6 ESMs in
427 simulating the effect of aerosols on terrestrial GPP. In this study, we showed that the
428 anthropogenic aerosols decreased the terrestrial GPP in all ESMs from 1850 to 2014
429 and the decreased GPP increased with the AOD. Zhang et al. (2023a) and Zhou et al.
430 (2024) also showed that the anthropogenic aerosols caused a reduction of terrestrial
431 carbon sink. This is generally consistent with the results in this study. However, Zhang
432 et al. (2021a) reported that anthropogenic aerosols increased terrestrial carbon sink by
433 22.6 PgC using ORCHIDEE_DF land components and IPSL-CM6A-LR climate and
434 aerosol forcing data. This bias might be induced through two pathways. First, AOD
435 from IPSL-CM6A-LR is lower than that from other models. Second, a new
436 development of ORCHIDEE trunk (ORCHIDEE_DF) with two-stream canopy light
437 transmission model was used, which can better capture the diffuse radiation fertilization
438 effect than the original IPSL-CM6A-LR model (Zhang et al., 2020).

439 **4.2 Ecosystem climate sensitivities of ESMs in CMIP6**

440 Our attribution framework reveals that the substantial inter-model spread in
441 aerosol-induced GPP anomalies is not merely caused by the divergent aerosol radiative
442 and climatic effects, but is also governed by the terrestrial ecosystem climate
443 sensitivities. This finding challenges the traditional view in improving simulating the
444 aerosol radiative and climatic effects alone and suggests that ecosystem climate
445 sensitivities of ESMs are also a dominant source of uncertainties in simulating aerosol-
446 induced GPP changes. Inter-model differences in ecosystem climate sensitivities
447 primarily came from the radiation and temperature sensitivities of photosynthesis in the
448 ESMs.



449 A critical source of divergence lies in the representation of canopy radiative transfer,
450 specifically the response to light quality. Compared to the MMM, UKESM1-0-LL
451 shows strong positive anomalies in the sensitivity to diffuse radiation. This behavior is
452 controlled by the land component (JULES). The model uses a multi-layer canopy
453 scheme with explicit light interception calculations for sunlit and shaded leaves at each
454 depth (Sellar et al., 2019; Clark et al., 2011). This canopy radiative transfer model
455 allows the diffuse radiation to reach the deeper canopy and can capture the DFE. The
456 IPSL-CM6A-LR shows the lowest DFE among all five models, because the model uses
457 a standard “big leaf” approach and does not consider the DFE (Cheruy et al., 2020;
458 Zhang et al., 2020). NorESM2-LM (CLM5) integrates a revised two-stream
459 approximation with the Medlyn stomatal conductance model (Lawrence et al., 2019).
460 This combination also can capture the DFE. However, this model shows lower DFE
461 than other models and this might be induced by the nutrient limitation.

462 Most land components of ESMs use the traditional Farquhar-Berry-Collatz
463 framework for simulating photosynthesis (Arora, 2003; Clark et al., 2011; Reick et al.,
464 2021; Boucher et al., 2020). However, there are large differences in how they consider
465 the influence of temperature on GPP. The impact of temperature on photosynthesis can
466 be divided into three parts, including chemical limits, adaptation to heat, and phenology.
467 For the level of immediate chemical reactions, the models have some differences in
468 estimating the response of V_{max} and J_{max} to temperature. MPI-ESM-1-2-HAM
469 (JSBACH 3.2) adopts a strict physical chemistry approach. The method uses the
470 Arrhenius equation and a specific inhibition function to calculate the impact of
471 temperature on key rates (Reick et al., 2021). When the temperature is higher than about
472 55°C, the photosynthetic rates will be zero. UKESM1-0-LL (JULES) adopts a formula
473 based on Q_{10} factors (Clark et al., 2011). At the level of adaptation to heat, NorESM2
474 (CLM5) introduces a mechanism for thermal acclimation based on the LUNA module
475 (Lawrence et al., 2019). BCC-ESM1 and IPSL-CM6A-LR use a traditional method,
476 which assumes that the response of plants to temperature is fixed (Boucher et al., 2020;
477 Li et al., 2019). CLM5 can adjust the nitrogen-use efficiency based on past



478 environmental conditions. Therefore, the photosynthetic capacity ($V_{\text{cmax}25}$) in the model
479 also changes dynamically. This will improve the accuracy of GPP in the area with big
480 seasonal changes and the photosynthesis in the model might be more sensitive to
481 warming than the model used traditional method. The plant phenology in BCC-ESM1
482 (BCC_AVIM2.0) is controlled by temperature (Li et al., 2019). The model adopts a
483 method based on accumulated heat to determine when leaves grow. This is different to
484 JSBACH, which uses chill days to break dormancy (Reick et al., 2021). Therefore,
485 BCC-ESM1 uses heat to support growth, while JSBACH focuses on the end of cold
486 days. This difference will lead to some divergences in predicting when the growing
487 season starts, especially in cold regions. In summary, these models use different
488 methods to estimate the impact of temperature on photosynthesis and this will lead to
489 the different response of GPP to temperature.

490 **4.3 Implications for future projections**

491 Our study suggests that there are some approaches to reduce uncertainty in
492 simulating the response of photosynthesis to aerosols. Of course, accurately estimating
493 the direct and indirect radiative effects of aerosols on GPP requires obtaining accurate
494 information about aerosol and gas emission, particulate growth, transport, and removal
495 (Li et al., 2022). Although refining atmospheric aerosol optical and microphysical
496 properties remains important, improving the simulation of terrestrial photosynthesis can
497 greatly reduce the model divergencies. First, canopy radiative transfer model should be
498 improved to estimate the impact of diffuse and direct radiation accurately. Some
499 parameters that affect canopy radiation transfer module should be incorporated into the
500 model. For example, Li et al. (2023) reported that the clumping index affects the light
501 environment within canopy. However, many ESMs do not incorporate the clumping
502 index and this will induce some uncertainties in simulating the canopy light
503 environment (Fang, 2021). Second, the acclimation of photosynthesis to soil moisture
504 and air temperature should be improved (Gabele et al., 2025). Although some models
505 have incorporated the acclimation of photosynthesis via various approaches, most of
506 the approaches were not sufficient to capture the full impact of air temperature and



507 water on photosynthesis. Ren et al. (2025) showed that the incorporation of eco-
508 evolutionary optimality (EEO) theories into model could improve photosynthesis
509 predictions. This might be an efficient way to improve the response of GPP to
510 precipitation and temperature.

511 **5. Summary**

512 Anthropogenic aerosol loadings have increased significantly since 1850. The
513 increased aerosols can significantly affect the terrestrial carbon cycle through reducing
514 the total shortwave radiation, increasing the diffuse radiation fraction, and altering the
515 temperature and precipitation. Many models were developed for simulating the effects
516 of aerosols on regional terrestrial carbon cycle. However, differences among models in
517 simulating the effects of aerosols on gross primary production (GPP) still need further
518 investigation. In this study, we investigated the differences in simulating the aerosol-
519 induced GPP changes among the models and the driving factors using five Earth System
520 Models (ESMs) from CMIP6, including BCC-ESM1, IPSL-CM6A-LR, MPI-ESM1-1-
521 2-HAM, NorESM2-LM, and UKESM1-0-LL. Our results indicated that all five models
522 simulated a reduction in global GPP. However, there are large uncertainties in the
523 magnitude and spatial distribution of these changes. Our results showed that inter-
524 model spread was mainly caused by terrestrial ecosystem climate sensitivities, rather
525 than atmospheric aerosol radiative and climatic effects in ESMs. Specifically, the
526 divergence was mainly induced by the different assumptions of canopy radiative
527 transfer and thermal acclimation. Our findings indicated that refining atmospheric
528 aerosol optical properties alone was insufficient to reduce uncertainties in simulating
529 aerosol-induced GPP changes. Future efforts must be used to improve the response of
530 photosynthesis to climatic factors.

531 **Code and data availability**

532 All model outputs from the Coupled Model Intercomparison Project Phase 6 (CMIP6)
533 (Earth System Grid Foundation, 2024) used in this paper are publicly available at
534 <https://aims2.llnl.gov/search/cmip6/> (Eyring et al., 2016). FLUXNET data are obtained
535 from Pastorello et al. (2020). FLUXCOM-X data can be accessed from the ICOS



536 Carbon Portal (Nelson et al., 2023). The post-processing scripts are available at
537 <https://doi.org/10.5281/zenodo.18396248> (Zhang, 2026).

538 **Author contributions**

539 Zhaoyang Zhang: Formal analysis; visualization; investigation; writing – original draft.
540 Meng Fan: Methodology; writing – review and editing. Minghui Tao, and Yunhui Tan:
541 Investigation. Quan Wang: writing – review and editing.

542 **Competing interests**

543 The contact author has declared that none of the authors has any competing interests.

544 **Financial support**

545 This work was supported by the National Natural Science Foundation of China (Grant
546 No. 42171366, 42375132, and 41801258).

547 **References**

- 548 Anav, A., Friedlingstein, P., Beer, C., Ciais, P., Harper, A., Jones, C., Murray-Tortarolo, G., Papale, D.,
549 Parazoo, N. C., Peylin, P., Piao, S. L., Sitch, S., Viovy, N., Wiltshire, A., and Zhao, M. S.: Spatiotemporal
550 patterns of terrestrial gross primary production: A review, *Reviews of Geophysics*, 53, 785-818,
551 <https://doi.org/10.1002/2015rg000483>, 2015.
- 552 Arora, V. K.: Simulating energy and carbon fluxes over winter wheat using coupled land surface
553 and terrestrial ecosystem models, *Agric. For. Meteorol.*, 118, 21-47,
554 [https://doi.org/10.1016/s0168-1923\(03\)00073-x](https://doi.org/10.1016/s0168-1923(03)00073-x), 2003.
- 555 Bellouin, N., Quaas, J., Gryspeerdt, E., Kinne, S., Stier, P., Watson-Parris, D., Boucher, O., Carslaw, K.
556 S., Christensen, M., Daniau, A. L., Dufresne, J. L., Feingold, G., Fiedler, S., Forster, P., Gettelman, A.,
557 Haywood, J. M., Lohmann, U., Malavelle, F., Mauritsen, T., McCoy, D. T., Myhre, G., Mulmenstadt,
558 J., Neubauer, D., Possner, A., Rugenstein, M., Sato, Y., Schulz, M., Schwartz, S. E., Sourdeval, O.,
559 Storelvmo, T., Toll, V., Winker, D., and Stevens, B.: Bounding Global Aerosol Radiative Forcing of
560 Climate Change, *Rev Geophys*, 58, e2019RG000660, <https://doi.org/10.1029/2019RG000660>, 2020.
- 561 Bloomfield, K. J., Stocker, B. D., Keenan, T. F., and Prentice, I. C.: Environmental controls on the light
562 use efficiency of terrestrial gross primary production, *Global Change Biol*, 29, 1037-1053,
563 <https://doi.org/10.1111/gcb.16511>, 2022.
- 564 Boucher, O., Servonnat, J., Albright, A. L., Aumont, O., Balkanski, Y., Bastrikov, V., Bekki, S., Bonnet,
565 R., Bony, S., Bopp, L., Braconnot, P., Brockmann, P., Cadule, P., Caubel, A., Cheruy, F., Codron, F.,
566 Cozic, A., Cugnet, D., D'Andrea, F., Davini, P., de Lavergne, C., Denvil, S., Deshayes, J., Devilliers, M.,
567 Ducharne, A., Dufresne, J. L., Dupont, E., Éthé, C., Fairhead, L., Falletti, L., Flavoni, S., Foujols, M. A.,
568 Gardoll, S., Gastineau, G., Ghattas, J., Grandpeix, J. Y., Guenet, B., Guez, L. E., Guilyardi, E.,
569 Guimberteau, M., Hauglustaine, D., Hourdin, F., Idelkadi, A., Joussaume, S., Kageyama, M., Khodri,
570 M., Krinner, G., Lebas, N., Levavasseur, G., Lévy, C., Li, L., Lott, F., Lurton, T., Luyssaert, S., Madec,
571 G., Madeleine, J. B., Maignan, F., Marchand, M., Marti, O., Mellul, L., Meurdesoif, Y., Mignot, J.,



572 Musat, I., Ottlé, C., Peylin, P., Planton, Y., Polcher, J., Rio, C., Rochetin, N., Rousset, C., Sepulchre, P.,
573 Sima, A., Swingedouw, D., Thiéblemont, R., Traore, A. K., Vancoppenolle, M., Vial, J., Vialard, J.,
574 Viovy, N., and Vuichard, N.: Presentation and Evaluation of the IPSL-CM6A-LR Climate Model,
575 Journal of Advances in Modeling Earth Systems, 12, <https://doi.org/10.1029/2019MS002010>, 2020.
576 Cheruy, F., Ducharne, A., Hourdin, F., Musat, I., Vignon, É., Gastineau, G., Bastrikov, V., Vuichard, N.,
577 Diallo, B., Dufresne, J. L., Ghattas, J., Grandpeix, J. Y., Idelkadi, A., Mellul, L., Maignan, F., Ménégoz,
578 M., Ottlé, C., Peylin, P., Servonnat, J., Wang, F., and Zhao, Y.: Improved Near-Surface Continental
579 Climate in IPSL-CM6A-LR by Combined Evolutions of Atmospheric and Land Surface Physics,
580 Journal of Advances in Modeling Earth Systems, 12, <https://doi.org/10.1029/2019MS002005>, 2020.
581 Clark, D. B., Mercado, L. M., Sitch, S., Jones, C. D., Gedney, N., Best, M. J., Pryor, M., Rooney, G. G.,
582 Essery, R. L. H., Blyth, E., Boucher, O., Harding, R. J., Huntingford, C., and Cox, P. M.: The Joint UK
583 Land Environment Simulator (JULES), model description - Part 2: Carbon fluxes and vegetation
584 dynamics, Geoscientific Model Development, 4, 701-722, [https://doi.org/10.5194/gmd-4-701-](https://doi.org/10.5194/gmd-4-701-2011)
585 [2011](https://doi.org/10.5194/gmd-4-701-2011), 2011.
586 Collins, W. J., Lamarque, J. F., Schulz, M., Boucher, O., Eyring, V., Hegglin, M. I., Maycock, A., Myhre,
587 G., Prather, M., Shindell, D., and Smith, S. J.: AerChemMIP: quantifying the effects of chemistry and
588 aerosols in CMIP6, Geoscientific Model Development, 10, 585-607, [https://doi.org/10.5194/gmd-](https://doi.org/10.5194/gmd-10-585-2017)
589 [10-585-2017](https://doi.org/10.5194/gmd-10-585-2017), 2017.
590 Earth System Grid Foundation: Earth System Grid Foundation (2024) [dataset], 2024.
591 Eyring, V., Bony, S., Meehl, G. A., Senior, C. A., Stevens, B., Stouffer, R. J., and Taylor, K. E.: Overview
592 of the Coupled Model Intercomparison Project Phase 6 (CMIP6) experimental design and
593 organization, Geoscientific Model Development, 9, 1937-1958, [https://doi.org/10.5194/gmd-9-](https://doi.org/10.5194/gmd-9-1937-2016)
594 [1937-2016](https://doi.org/10.5194/gmd-9-1937-2016), 2016.
595 Fang, H. L.: Canopy clumping index (CI): A review of methods, characteristics, and applications,
596 Agric. For. Meteorol., 303, 108374, <https://doi.org/10.1016/j.agrformet.2021.108374>, 2021.
597 Gabele, L. M., Sieber, P., Liu, L., and Seneviratne, S. I.: Soil moisture-induced changes in land carbon
598 sink projections in CMIP6, EGU sphere, 2025, 1-23, <https://doi.org/10.5194/egusphere-2025-4215>,
599 2025.
600 Gier, B. K., Schlund, M., Friedlingstein, P., Jones, C. D., Jones, C., Zaehle, S., and Eyring, V.:
601 Representation of the terrestrial carbon cycle in CMIP6, Biogeosciences, 21, 5321-5360,
602 <https://doi.org/10.5194/bg-21-5321-2024>, 2024.
603 Gu, L., Baldocchi, D., Verma, S. B., Black, T. A., Vesala, T., Falge, E. M., and Dowty, P. R.: Advantages
604 of diffuse radiation for terrestrial ecosystem productivity, Journal of Geophysical Research:
605 Atmospheres, 107, ACL 2-1-ACL 2-23, <https://doi.org/10.1029/2001jd001242>, 2002.
606 Gu, L., Baldocchi, D. D., Wofsy, S. C., Munger, J. W., Michalsky, J. J., Urbanski, S. P., and Boden, T.
607 A.: Response of a deciduous forest to the Mount Pinatubo eruption: enhanced photosynthesis,
608 Science, 299, 2035-2038, <https://doi.org/10.1126/science.1078366>, 2003.
609 Hu, Q., Li, T., Deng, X., Wu, T., Zhai, P., Huang, D., Fan, X., Zhu, Y., Lin, Y., Xiao, X., Chen, X., Zhao,
610 X., Wang, L., and Qin, Z.: Intercomparison of global terrestrial carbon fluxes estimated by MODIS
611 and Earth system models, Sci. Total Environ., 810, 152231,
612 <https://doi.org/10.1016/j.scitotenv.2021.152231>, 2022.
613 Huang, M., Piao, S., Ciais, P., Penuelas, J., Wang, X., Keenan, T. F., Peng, S., Berry, J. A., Wang, K.,
614 Mao, J., Alkama, R., Cescatti, A., Cuntz, M., De Deurwaerder, H., Gao, M., He, Y., Liu, Y., Luo, Y.,
615 Myneni, R. B., Niu, S., Shi, X., Yuan, W., Verbeeck, H., Wang, T., Wu, J., and Janssens, I. A.: Air



- 616 temperature optima of vegetation productivity across global biomes, *Nat Ecol Evol*, 3, 772-779,
617 <https://doi.org/10.1038/s41559-019-0838-x>, 2019.
- 618 Khatri, P., Hayasaka, T., Holben, B., Tripathi, S. N., Misra, P., Patra, P. K., Hayashida, S., and Dumka,
619 U. C.: Aerosol Loading and Radiation Budget Perturbations in Densely Populated and Highly
620 Polluted Indo-Gangetic Plain by COVID-19: Influences on Cloud Properties and Air Temperature,
621 *Geophys. Res. Lett.*, 48, e2021GL093796, <https://doi.org/10.1029/2021GL093796>, 2021.
- 622 Lai, J., Kooijmans, L. M. J., Sun, W., Lombardozi, D., Campbell, J. E., Gu, L., Luo, Y., Kuai, L., and
623 Sun, Y.: Terrestrial photosynthesis inferred from plant carbonyl sulfide uptake, *Nature*,
624 <https://doi.org/10.1038/s41586-024-08050-3>, 2024.
- 625 Lasslop, G., Reichstein, M., Papale, D., Richardson, A. D., Arneeth, A., Barr, A., Stoy, P., and Wohlfahrt,
626 G.: Separation of net ecosystem exchange into assimilation and respiration using a light response
627 curve approach: critical issues and global evaluation, *Global Change Biol*, 16, 187-208,
628 <https://doi.org/10.1111/j.1365-2486.2009.02041.x>, 2010.
- 629 Lawrence, D. M., Oleson, K. W., Flanner, M. G., Thornton, P. E., Swenson, S. C., Lawrence, P. J., Zeng,
630 X., Yang, Z.-L., Levis, S., Sakaguchi, K., Bonan, G. B., and Slater, A. G.: Parameterization
631 improvements and functional and structural advances in Version 4 of the Community Land Model,
632 *Journal of Advances in Modeling Earth Systems*, 3, 1-27, <https://doi.org/10.1029/2011ms000045>,
633 2011.
- 634 Lawrence, D. M., Fisher, R. A., Koven, C. D., Oleson, K. W., Swenson, S. C., Bonan, G., Collier, N.,
635 Ghimire, B., van Kampenhout, L., Kennedy, D., Kluzek, E., Lawrence, P. J., Li, F., Li, H., Lombardozi,
636 D., Riley, W. J., Sacks, W. J., Shi, M., Vertenstein, M., Wieder, W. R., Xu, C., Ali, A. A., Badger, A. M.,
637 Bisht, G., van den Broeke, M., Brunke, M. A., Burns, S. P., Buzan, J., Clark, M., Craig, A., Dahlin, K.,
638 Drewniak, B., Fisher, J. B., Flanner, M., Fox, A. M., Gentine, P., Hoffman, F., Keppel-Aleks, G., Knox,
639 R., Kumar, S., Lenaerts, J., Leung, L. R., Lipscomb, W. H., Lu, Y., Pandey, A., Pelletier, J. D., Perket, J.,
640 Randerson, J. T., Ricciuto, D. M., Sanderson, B. M., Slater, A., Subin, Z. M., Tang, J., Thomas, R. Q.,
641 Val Martin, M., and Zeng, X.: The Community Land Model Version 5: Description of New Features,
642 Benchmarking, and Impact of Forcing Uncertainty, *Journal of Advances in Modeling Earth Systems*,
643 11, 4245-4287, <https://doi.org/10.1029/2018MS001583>, 2019.
- 644 Leung, G. R. and van den Heever, S. C.: Aerosol breezes drive cloud and precipitation increases,
645 *Nat. Commun.*, 14, 2508, <https://doi.org/10.1038/s41467-023-37722-3>, 2023.
- 646 Li, F., Hao, D., Zhu, Q., Yuan, K., Braghieri, R. K., He, L., Luo, X., Wei, S., Riley, W. J., Zeng, Y., and
647 Chen, M.: Vegetation clumping modulates global photosynthesis through adjusting canopy light
648 environment, *Glob Chang Biol*, 29, 731-746, <https://doi.org/10.1111/gcb.16503>, 2023.
- 649 Li, J., Carlson, B. E., Yung, Y. L., Lv, D. R., Hansen, J., Penner, J. E., Liao, H., Ramaswamy, Kahn, R. A.,
650 Zhang, P., Dubovik, O., Ding, A. J., Laci, A. A., Zhang, L., and Dong, Y. M.: Scattering and absorbing
651 aerosols in the climate system, *Nature Reviews Earth & Environment*, 3, 363-379,
652 <https://doi.org/10.1038/s43017-022-00296-7>, 2022.
- 653 Li, W. P., Zhang, Y. W., Shi, X. L., Zhou, W. Y., Huang, A. N., Mu, M. Q., Qiu, B., and Ji, J. J.:
654 Development of Land Surface Model BCC_AVIM2.0 and Its Preliminary Performance in
655 LS3MIP/CMIP6, *Journal of Meteorological Research*, 33, 851-869,
656 <https://doi.org/10.1007/s13351-019-9016-y>, 2019.
- 657 Liu, Q. Z., Zhang, Z. Y., Fan, M., and Wang, Q.: The Divergent Estimates of Diffuse Radiation Effects
658 on Gross Primary Production of Forest Ecosystems Using Light-Use Efficiency Models, *Geophys.*
659 *Res. Lett.*, 48, e2021GL093864, <https://doi.org/10.1029/2021GL093864>, 2021.



660 Liu, Z. C., Lang, X. M., and Jiang, D. B.: Impact of stratospheric aerosol intervention geoengineering
661 on surface air temperature in China: a surface energy budget perspective, *Atmos. Chem. Phys.*, 22,
662 7667-7680, <https://doi.org/10.5194/acp-22-7667-2022>, 2022.

663 Mauritsen, T., Bader, J., Becker, T., Behrens, J., Bittner, M., Brokopf, R., Brovkin, V., Claussen, M.,
664 Crueger, T., Esch, M., Fast, I., Fiedler, S., Flaschner, D., Gayler, V., Giorgetta, M., Goll, D. S., Haak, H.,
665 Hagemann, S., Hedemann, C., Hohenegger, C., Ilyina, T., Jahns, T., Jimenez-de-la-Cuesta, D.,
666 Jungclaus, J., Kleinen, T., Kloster, S., Kracher, D., Kinne, S., Kleberg, D., Lasslop, G., Kornblueh, L.,
667 Marotzke, J., Matei, D., Meraner, K., Mikolajewicz, U., Modali, K., Mobis, B., Muller, W. A., Nabel, J.,
668 Nam, C. C. W., Notz, D., Nyawira, S. S., Paulsen, H., Peters, K., Pincus, R., Pohlmann, H., Pongratz,
669 J., Popp, M., Raddatz, T. J., Rast, S., Redler, R., Reick, C. H., Rohrschneider, T., Schemann, V., Schmidt,
670 H., Schnur, R., Schulzweida, U., Six, K. D., Stein, L., Stemmler, I., Stevens, B., von Storch, J. S., Tian,
671 F., Voigt, A., Vrese, P., Wieners, K. H., Wilkenskeld, S., Winkler, A., and Roeckner, E.: Developments
672 in the MPI-M Earth System Model version 1.2 (MPI-ESM1.2) and Its Response to Increasing CO₂,
673 *J Adv Model Earth Syst*, 11, 998-1038, <https://doi.org/10.1029/2018MS001400>, 2019.

674 Mercado, L. M., Bellouin, N., Sitch, S., Boucher, O., Huntingford, C., Wild, M., and Cox, P. M.: Impact
675 of changes in diffuse radiation on the global land carbon sink, *Nature*, 458, 1014-1017,
676 <https://doi.org/10.1038/nature07949>, 2009.

677 Najafi, M. R., Zwiers, F. W., and Gillett, N. P.: Attribution of Arctic temperature change to
678 greenhouse-gas and aerosol influences, *Nature Climate Change*, 5, 246-249,
679 <https://doi.org/10.1038/Nclimate2524>, 2015.

680 Nelson, J. A., Walther, S., Jung, M., Gans, F., Kraft, B., Weber, U., Hamdi, Z., Duveiller, G., and Zhang,
681 W.: FLUXCOM-X-BASE [dataset], <https://doi.org/10.18160/5NZG-JMJE>, 2023.

682 Nelson, J. A., Walther, S., Gans, F., Kraft, B., Weber, U., Novick, K., Buchmann, N., Migliavacca, M.,
683 Wohlfahrt, G., Šigut, L., Ibrom, A., Papale, D., Göckede, M., Duveiller, G., Knohl, A., Hörtnagl, L.,
684 Scott, R. L., Zhang, W., Hamdi, Z. M., Reichstein, M., Aranda-Barranco, S., Ardö, J., Op de Beeck,
685 M., Billdesbach, D., Bowling, D., Bracho, R., Brümmer, C., Camps-Valls, G., Chen, S., Cleverly, J. R.,
686 Desai, A., Dong, G., El-Madany, T. S., Euskirchen, E. S., Feigenwinter, I., Galvagno, M., Gerosa, G.,
687 Gielen, B., Goded, I., Goslee, S., Gough, C. M., Heinesch, B., Ichii, K., Jackowicz-Korczynski, M. A.,
688 Klosterhalfen, A., Knox, S., Kobayashi, H., Kohonen, K. M., Korkiakoski, M., Mammarella, I., Mana,
689 G., Marzuoli, R., Matamala, R., Metzger, S., Montagnani, L., Nicolini, G., O'Halloran, T., Ourcival, J.
690 M., Peichl, M., Pendall, E., Ruiz Reverter, B., Roland, M., Sabbatini, S., Sachs, T., Schmidt, M.,
691 Schwalm, C. R., Shekhar, A., Silberstein, R., Silveira, M. L., Spano, D., Tagesson, T., Tramontana, G.,
692 Trotta, C., Turco, F., Vesala, T., Vincke, C., Vitale, D., Vivoni, E. R., Wang, Y., Woodgate, W., Yopez,
693 E. A., Zhang, J., Zona, D., and Jung, M.: X-BASE: the first terrestrial carbon and water flux products
694 from an extended data-driven scaling framework, *FLUXCOM-X*, *EGUsphere*, 2024, 1-51,
695 <https://doi.org/10.5194/egusphere-2024-165>, 2024.

696 Niyogi, D., Chang, H. I., Saxena, V. K., Holt, T., Alapaty, K., Booker, F., Chen, F., Davis, K. J., Holben,
697 B., Matsui, T., Meyers, T., Oechel, W. C., Pielke, R. A., Wells, R., Wilson, K., and Xue, Y.: Direct
698 observations of the effects of aerosol loading on net ecosystem CO₂ exchanges over different
699 landscapes, *Geophys. Res. Lett.*, 31, <https://doi.org/10.1029/2004gl020915>, 2004.

700 Pastorello, G., Trotta, C., Canfora, E., Chu, H., Christianson, D., Cheah, Y. W., Poindexter, C., Chen,
701 J., Elbashandy, A., Humphrey, M., Isaac, P., Polidori, D., Reichstein, M., Ribeca, A., van Ingen, C.,
702 Vuichard, N., Zhang, L., Amiro, B., Ammann, C., Arain, M. A., Ardo, J., Arkebauer, T., Arndt, S. K.,
703 Arriga, N., Aubinet, M., Aurela, M., Baldocchi, D., Barr, A., Beamesderfer, E., Marchesini, L. B.,



704 Bergeron, O., Beringer, J., Bernhofer, C., Berveiller, D., Billesbach, D., Black, T. A., Blanken, P. D.,
705 Bohrer, G., Boike, J., Bolstad, P. V., Bonal, D., Bonnefond, J. M., Bowling, D. R., Bracho, R., Brodeur,
706 J., Brummer, C., Buchmann, N., Burban, B., Burns, S. P., Buysse, P., Cale, P., Cavagna, M., Cellier, P.,
707 Chen, S., Chini, I., Christensen, T. R., Cleverly, J., Collalti, A., Consalvo, C., Cook, B. D., Cook, D.,
708 Coursolle, C., Cremonese, E., Curtis, P. S., D'Andrea, E., da Rocha, H., Dai, X., Davis, K. J., Cinti, B.,
709 Grandcourt, A., Ligne, A., De Oliveira, R. C., Delpierre, N., Desai, A. R., Di Bella, C. M., Tommasi, P.
710 D., Dolman, H., Domingo, F., Dong, G., Dore, S., Duce, P., Dufrene, E., Dunn, A., Dusek, J., Eamus,
711 D., Eichelmann, U., ElKhidir, H. A. M., Eugster, W., Ewenz, C. M., Ewers, B., Famulari, D., Fares, S.,
712 Feigenwinter, I., Feitz, A., Fensholt, R., Filippa, G., Fischer, M., Frank, J., Galvagno, M., Gharun, M.,
713 Gianelle, D., Gielen, B., Gioli, B., Gitelson, A., Goded, I., Goeckede, M., Goldstein, A. H., Gough, C.
714 M., Goulden, M. L., Graf, A., Griebel, A., Gruening, C., Grunwald, T., Hammerle, A., Han, S., Han, X.,
715 Hansen, B. U., Hanson, C., Hatakka, J., He, Y., Hehn, M., Heinesch, B., Hinko-Najera, N., Hortnagl,
716 L., Hutley, L., Ibrom, A., Ikawa, H., Jackowicz-Korczynski, M., Janous, D., Jans, W., Jassal, R., Jiang,
717 S., Kato, T., Khomik, M., Klatt, J., Knohl, A., Knox, S., Kobayashi, H., Koerber, G., Kolle, O., Kosugi, Y.,
718 Kotani, A., Kowalski, A., Kruijt, B., Kurbatova, J., Kutsch, W. L., Kwon, H., Launiainen, S., Laurila, T.,
719 Law, B., Leuning, R., Li, Y., Liddell, M., Limousin, J. M., Lion, M., Liska, A. J., Lohila, A., Lopez-
720 Ballesteros, A., Lopez-Blanco, E., Loubet, B., Loustau, D., Lucas-Moffat, A., Luers, J., Ma, S.,
721 Macfarlane, C., Magliulo, V., Maier, R., Mammarella, I., Manca, G., Marcolla, B., Margolis, H. A.,
722 Marras, S., Massman, W., Mastepanov, M., Matamala, R., Matthes, J. H., Mazzenga, F., McCaughey,
723 H., McHugh, I., McMillan, A. M. S., Merbold, L., Meyer, W., Meyers, T., Miller, S. D., Minerbi, S.,
724 Moderow, U., Monson, R. K., Montagnani, L., Moore, C. E., Moors, E., Moreaux, V., Moureaux, C.,
725 Munger, J. W., Nakai, T., Neiryneck, J., Nestic, Z., Nicolini, G., Noormets, A., Northwood, M., Nosetto,
726 M., Nouvellon, Y., Novick, K., Oechel, W., Olesen, J. E., Ourcival, J. M., Papuga, S. A., Parmentier, F.
727 J., Paul-Limoges, E., Pavelka, M., Peichl, M., Pendall, E., Phillips, R. P., Pilegaard, K., Pirk, N., Posse,
728 G., Powell, T., Prasse, H., Prober, S. M., Rambal, S., Rannik, U., Raz-Yaseef, N., Rebmann, C., Reed,
729 D., Dios, V. R., Restrepo-Coupe, N., Reverter, B. R., Roland, M., Sabbatini, S., Sachs, T., Saleska, S.
730 R., Sanchez-Canete, E. P., Sanchez-Mejia, Z. M., Schmid, H. P., Schmidt, M., Schneider, K., Schrader,
731 F., Schroder, I., Scott, R. L., Sedlak, P., Serrano-Ortiz, P., Shao, C., Shi, P., Shironya, I., Siebicke, L.,
732 Sigut, L., Silberstein, R., Sirca, C., Spano, D., Steinbrecher, R., Stevens, R. M., Sturtevant, C., Suyker,
733 A., Tagesson, T., Takahashi, S., Tang, Y., Tapper, N., Thom, J., Tomassucci, M., Tuovinen, J. P.,
734 Urbanski, S., Valentini, R., van der Molen, M., van Gorsel, E., van Huissteden, K., Varlagin, A.,
735 Verfaillie, J., Vesala, T., Vincke, C., Vitale, D., Vygodskaya, N., Walker, J. P., Walter-Shea, E., Wang,
736 H., Weber, R., Westermann, S., Wille, C., Wofsy, S., Wohlfahrt, G., Wolf, S., Woodgate, W., Li, Y.,
737 Zampedri, R., Zhang, J., Zhou, G., Zona, D., Agarwal, D., Biraud, S., Torn, M., and Papale, D.: The
738 FLUXNET2015 dataset and the ONEFlux processing pipeline for eddy covariance data, *Sci Data*, 7,
739 225, <https://doi.org/10.1038/s41597-020-0534-3>, 2020.

740 Piao, S., Ciais, P., Friedlingstein, P., Peylin, P., Reichstein, M., Luysaert, S., Margolis, H., Fang, J., Barr,
741 A., Chen, A., Grelle, A., Hollinger, D. Y., Laurila, T., Lindroth, A., Richardson, A. D., and Vesala, T.:
742 Net carbon dioxide losses of northern ecosystems in response to autumn warming, *Nature*, 451,
743 49-52, <https://doi.org/10.1038/nature06444>, 2008.

744 Rap, A., Scott, C. E., Reddington, C. L., Mercado, L., Ellis, R. J., Garraway, S., Evans, M. J., Beerling, D.
745 J., MacKenzie, A. R., Hewitt, C. N., and Spracklen, D. V.: Enhanced global primary production by
746 biogenic aerosol via diffuse radiation fertilization, *Nature Geoscience*, 11, 640-+,
747 <https://doi.org/10.1038/s41561-018-0208-3>, 2018.



- 748 Reick, C. H., Gayler, V., Goll, D., Hagemann, S., Heidkamp, M., Nabel, J. E. M. S., Raddatz, T.,
749 Roeckner, E., Schnur, R., and Wilkenskjeld, S.: JSBACH 3 - The land component of the MPI Earth
750 System Model: documentation of version 3.2, MPI für Meteorologie,
751 <https://doi.org/10.17617/2.3279802>, 2021.
- 752 Ren, Y. H., Wang, H., Harrison, S. P., Prentice, I. C., Mengoli, G., Zhao, L., Reich, P. B., and Yang, K.:
753 Incorporating the Acclimation of Photosynthesis and Leaf Respiration in the Noah-MP Land
754 Surface Model: Model Development and Evaluation, *Journal of Advances in Modeling Earth
755 Systems*, 17, <https://doi.org/10.1029/2024MS004599>, 2025.
- 756 Sellar, A. A., Jones, C. G., Mulcahy, J. P., Tang, Y., Yool, A., Wiltshire, A., O'Connor, F. M., Stringer,
757 M., Hill, R., Palmieri, J., Woodward, S., de Mora, L., Kuhlbrodt, T., Rumbold, S. T., Kelley, D. I., Ellis,
758 R., Johnson, C. E., Walton, J., Abraham, N. L., Andrews, M. B., Andrews, T., Archibald, A. T., Berthou,
759 S., Burke, E., Blockley, E., Carslaw, K., Dalvi, M., Edwards, J., Folberth, G. A., Gedney, N., Griffiths, P.
760 T., Harper, A. B., Hendry, M. A., Hewitt, A. J., Johnson, B., Jones, A., Jones, C. D., Keeble, J., Liddicoat,
761 S., Morgenstern, O., Parker, R. J., Predoi, V., Robertson, E., Siahhaan, A., Smith, R. S., Swaminathan,
762 R., Woodhouse, M. T., Zeng, G., and Zerroukat, M.: UKESM1: Description and Evaluation of the U.K.
763 Earth System Model, *Journal of Advances in Modeling Earth Systems*, 11, 4513-4558,
764 <https://doi.org/10.1029/2019MS001739>, 2019.
- 765 Shao, L., Li, G., Zhao, Q., Li, Y., Sun, Y., Wang, W., Cai, C., Chen, W., Liu, R., Luo, W., Yin, X., and Lee,
766 X.: The fertilization effect of global dimming on crop yields is not attributed to an improved light
767 interception, *Glob Chang Biol*, 26, 1697-1713, <https://doi.org/10.1111/gcb.14822>, 2020.
- 768 Tan, Y. H., Wang, Q., and Zhang, Z. Y.: Near-real-time estimation of global horizontal irradiance
769 from Himawari-8 satellite data, *Renewable Energy*, 215, 118994,
770 <https://doi.org/10.1016/j.renene.2023.118994>, 2023.
- 771 Wang, X., Wu, J., Chen, M., Xu, X., Wang, Z., Wang, B., Wang, C., Piao, S., Lin, W., Miao, G., Deng,
772 M., Qiao, C., Wang, J., Xu, S., and Liu, L.: Field evidences for the positive effects of aerosols on tree
773 growth, *Glob Chang Biol*, 24, 4983-4992, <https://doi.org/10.1111/gcb.14339>, 2018.
- 774 Wu, D., Yuan, T., Zhang, J., Zhang, Z., Zhang, D., Zhang, B., Liu, J., Pu, W., and Wang, X.: Contrasting
775 Responses of Smoke Dispersion and Fire Emissions to Aerosol-Radiation Interaction during the
776 Largest Australian Wildfires in 2019-2020, *Environ Sci Technol*, 59, 1724-1736,
777 <https://doi.org/10.1021/acs.est.4c12034>, 2025.
- 778 Wu, T. W., Zhang, F., Zhang, J., Jie, W. H., Zhang, Y. W., Wu, F. H., Li, L., Yan, J. H., Liu, X. H., Lu, X.,
779 Tan, H. Y., Zhang, L., Wang, J., and Hu, A. X.: Beijing Climate Center Earth System Model version 1
780 (BCC-ESM1): model description and evaluation of aerosol simulations, *Geoscientific Model
781 Development*, 13, 977-1005, <https://doi.org/10.5194/gmd-13-977-2020>, 2020.
- 782 Yu, Q. and Huang, Y.: Distributions and Trends of the Aerosol Direct Radiative Effect in the 21st
783 Century: Aerosol and Environmental Contributions, *Journal of Geophysical Research: Atmospheres*,
784 128, <https://doi.org/10.1029/2022jd037716>, 2023.
- 785 Yue, X. and Unger, N.: Aerosol optical depth thresholds as a tool to assess diffuse radiation
786 fertilization of the land carbon uptake in China, *Atmos. Chem. Phys.*, 17, 1329-1342,
787 <https://doi.org/10.5194/acp-17-1329-2017>, 2017.
- 788 Zhang, H. W., Li, L. H., Song, J., Akhter, Z. H., and Zhang, J. J.: Understanding aerosol-climate-
789 ecosystem interactions and the implications for terrestrial carbon sink using the Community Earth
790 System Model, *Agric. For. Meteorol.*, 340, 109625,
791 <https://doi.org/10.1016/j.agrformet.2023.109625>, 2023a.



792 Zhang, Y., Ciais, P., Boucher, O., Maignan, F., Bastos, A., Goll, D., Lurton, T., Viovy, N., Bellouin, N.,
793 and Li, L.: Disentangling the Impacts of Anthropogenic Aerosols on Terrestrial Carbon Cycle During
794 1850–2014, *Earths Future*, 9, e2021EF002035, <https://doi.org/10.1029/2021EF002035>, 2021a.
795 Zhang, Y., Goll, D., Bastos, A., Balkanski, Y., Boucher, O., Cescatti, A., Collier, M., Gasser, T., Ghattas,
796 J., Li, L., Piao, S., Viovy, N., Zhu, D., and Ciais, P.: Increased Global Land Carbon Sink Due to Aerosol-
797 Induced Cooling, *Global Biogeochem. Cycles*, 33, 439–457,
798 <https://doi.org/10.1029/2018gb006051>, 2019.
799 Zhang, Y., Bastos, A., Maignan, F., Goll, D., Boucher, O., Li, L., Cescatti, A., Vuichard, N., Chen, X. Z.,
800 Ammann, C., Arain, M. A., Black, T. A., Chojnicki, B., Kato, T., Mammarella, I., Montagnani, L.,
801 Rouspard, O., Sanz, M. J., Siebicke, L., Urbaniak, M., Vaccari, F. P., Wohlfahrt, G., Woodgate, W.,
802 and Ciais, P.: Modeling the impacts of diffuse light fraction on photosynthesis in ORCHIDEE (v5453)
803 land surface model, *Geoscientific Model Development*, 13, 5401–5423,
804 <https://doi.org/10.5194/gmd-13-5401-2020>, 2020.
805 Zhang, Z.: Post-processing scripts for "Ecosystem Climate Sensitivities Drive the Divergence in
806 Aerosol-Induced Carbon Uptake Across CMIP6 Models", Zenodo [code],
807 <https://doi.org/10.5281/zenodo.18396247>, 2026.
808 Zhang, Z., Xiong, J., Fan, M., Tao, M., Wang, Q., and Bai, Y.: Satellite-observed vegetation responses
809 to aerosols variability, *Agric. For. Meteorol.*, 329, 109278,
810 <https://doi.org/10.1016/j.agrformet.2022.109278>, 2023b.
811 Zhang, Z. Y., Liu, Q. Z., Ruan, Y. C., and Tan, Y. H.: Estimation of aerosol radiative effects on
812 terrestrial gross primary productivity and water use efficiency using process-based model and
813 satellite data, *Atmospheric Research*, 247, 105245,
814 <https://doi.org/10.1016/j.atmosres.2020.105245>, 2021b.
815 Zhang, Z. Y., Fan, M., Tao, M. H., Tan, Y. H., and Wang, Q.: Large Divergence of Satellite Monitoring
816 of Diffuse Radiation Effect on Ecosystem Water-Use Efficiency, *Geophys. Res. Lett.*, 50,
817 e2023GL106086, <https://doi.org/10.1029/2023GL106086>, 2023c.
818 Zhang, Z. Y., Zhu, K. L., Fan, M., Wang, Q., and Tan, Y. H.: Diffuse Fertilization Effect in Maize and
819 Soybean Is Driven by Improved Light Use Efficiency Rather Than by Light Absorption, *J Geophys*
820 *Res-Bioge*, 129, <https://doi.org/10.1029/2023JG007766>, 2024.
821 Zhou, H., Yue, X., Dai, H. B., Geng, G. N., Yuan, W. P., Chen, J. Q., Shen, G. F., Zhang, T. Y., Zhu, J.,
822 and Liao, H.: Recovery of ecosystem productivity in China due to the Clean Air Action plan, *Nature*
823 *Geoscience*, 17, <https://doi.org/10.1038/s41561-024-01586-z>, 2024.

824